



Flexible, compressible, versatile biomass-derived freestanding carbon monoliths as binder- and substrate-free tri-functional electrodes for solid-state zinc-air batteries and overall water splitting

Hong Jin Son, Ye Rim Cho, Ye-Eun Park, Sung Hoon Ahn^{*}

Department of Bio-Chemical and Polymer Engineering, Chosun University, 309 Pilmun-daero, Dong-gu, Gwangju 61452, South Korea

ARTICLE INFO

Keywords:

Biomass-derived
Freestanding
Compressible electrode
Flexible electrode
Tri-functional

ABSTRACT

Highly flexible and compressible biomass-derived freestanding monoliths are directly utilized as binder- and substrate-free tri-functional electrodes for the wearable electronic devices. The introduction of Co nanoparticles, nanoclusters, and single atoms onto biomass-derived monoliths leads to the additional growth of CNTs for ensuring the interconnectivity of 3D cellulose-derived carbon network. Thus, superb flexibility and/or compressibility as well as high-efficiency tri-functional activity are achieved simultaneously. The alkaline water electrolyzer with monolithic electrodes requires only a potential of 1.56 V to generate hydrogen at a current density of 50 mA cm⁻² for over 120 h. Furthermore, the quasi-solid-state zinc-air batteries (ZABs) exhibit a high peak power density of 175.5 mW cm⁻², and an optimal charge-discharge overpotential with a remarkably small voltage gap (ΔV) of 0.27 V at 5 mA cm⁻². The excellent charge-discharge cycle stability even under bending and compression conditions demonstrates its high potential for emerging next-generation electronics devices.

1. Introduction

Carbon-rich biomass can be converted directly into carbonaceous nanomaterials while maintaining its original nanostructure, thus it is great of interest as electrode materials for energy conversion and storage devices [1,2]. For instance, some biomass can be converted into activated carbon materials, known as “biochar” by a pyrolysis process in the absence of oxygen [3,4]. This eco-friendly and relatively inexpensive biomass-derived carbon can further increase the cost-effectiveness of energy systems by replacing expansive carbon nanomaterials such as commercial carbon nanotubes (CNTs) and graphene. However, pure carbon nanomaterials exhibit benign activity as the electrocatalysts towards most electrochemical reactions, such as the oxygen evolution reaction (OER), hydrogen evolution reaction (HER), and oxygen reduction reaction (ORR). In some pioneer studies, metal-free nitrogen-doped porous carbon nanomaterials derived from biomass such as silk [5,6] has been proven to catalyze ORR in an alkaline electrolyte, thus regarded as an electrode material for fuel cells and zinc-air batteries (ZABs). Furthermore, the introduction of heteroatoms such as nitrogen along with metal species [7,8] into biomass-derived carbon electrocatalysts endows multi-functional activity to simultaneously promotes the multiple reactions. In particular, the combination of nitrogen-doped

carbon matrix with transition metal species leads to the formation of metal-nitrogen (M-N_x, M = Co, Ni, Fe, Cu) moieties as the active sites for multiple electrochemical reactions. The appropriate binding energy of M-N_x moieties toward the intermediates of the electrochemical reactions were theoretically predicted with first-principles density functional theory (DFT) calculations and the practical multi-functional activities were experimentally investigated [9,10]. Therefore, nitrogen- and/or metal-incorporated carbon electrocatalysts from various kinds of biomass such as wood [11], bacterial cellulose [12], chitosan [13], silk [14] have been reported, prepared by an activation process such as micro/nano-level pulverization, introduction of heteroatoms and/or metal species, and pyrolysis processes.

To date, intensive efforts have been focused on developing the self-supporting electrodes to improve the catalytic activity while lowering the total cost by simplifying the complicated manufacturing process [15]. Typically, the self-supporting electrodes can be prepared by directly growing a nanostructured catalyst material on the pre-existing substrates. However, the catalytic activity of the electrodes is often limited by the choice of pre-existing substrates with fixed factors such as three-dimensional (3D) structure, size and thickness, and even flexibility or compressibility. As a more advanced electrode design, a freestanding electrode has been proposed, i.e., self-standing electrode, in which the

^{*} Corresponding author.

E-mail address: sunghoon@chosun.ac.kr (S.H. Ahn).

<https://doi.org/10.1016/j.apcatb.2021.120977>

Received 1 September 2021; Received in revised form 11 November 2021; Accepted 26 November 2021

Available online 27 November 2021

0926-3373/© 2021 Elsevier B.V. All rights reserved.

active material itself constitutes an electrode without a pre-existing substrate. As a practical electrode for energy devices, large amounts of active materials can be loaded on freestanding electrode while minimizing the interfacial formation between the pre-existing substrate and the active material. As a catalytic electrode in alkaline water electrolyzer for overall water splitting (OWS), biomass-derived carbon electrodes possess abundant active sites in fully developed pore structures, exhibiting high catalytic activity and robust long-term durability for mass production of hydrogen gas [16]. Similarly, porous 3D electrodes as air cathodes for zinc-air batteries (ZABs) can greatly improve both the initial voltage gap of the charge-discharge polarization curve and cycle durability by creating a 3D reactive region [17–20]. In both energy systems, freestanding electrode with 3D porous structure is considered the most promising electrode design for optimizing the initial performance and durability of the system.

The high flexibility and/or compressibility of free-standing electrodes endows new form factors for next-generation electronic devices, including ZABs. Most of the previously reported flexible electrodes are based on the inherent flexibility of supporting substrates such as nickel foam and carbon cloth. Cheng et al. have reported a flexible 3D bi-functional electrode by coupling nickel-iron (NiFe) nanoparticles and N-doped carbon nanofibers on flexible carbon cloth substrate [21]. Similarly, nitrogen and cobalt co-doped carbon nanotube films directly grown on carbon cloth [22], and $(\text{Ni}, \text{Co})_3\text{O}_4$ nanosheets grown on nickel foam [23] have been reported as flexible self-supporting electrodes for quasi-solid-state ZABs. However, these self-supporting electrodes still require an additional supporting substrate and rely primarily on the inherent flexibility of the substrate rather than the catalytic nanomaterial itself. In this case, structural damage of the active material under mechanical deformation conditions such as bending or compression leads to degradation of catalyst activity and system performance. Some low-dimensional building blocks, such as 1D electro-spun nanofibers and two-dimensional (2D) graphene, can self-assemble to construct freestanding monolithic carbon electrodes, while the mechanical strength of the electrodes is generally not sufficient and they lack flexibility and elasticity [24]. To date, the compressibility control of ZABs has been mainly derived from elastic hydrogel electrolyte [25], and there are only a few studies of ZABs with compressible electrodes [26–28]. The recovery from mechanical deformation is highly dependent on the interaction of building blocks, and the introduction of 1D nanomaterials such as carbon nanotubes or nanofibers is effective in improving the mechanical strength of carbon aerogel. Similarly, additional “glue” such as carbon precursors and/or cellulose nanomaterials can be introduced to improve the interconnectivity of the building blocks [29].

In this study, we propose a novel synthetic approach of the direct conversion from miscanthus stem to freestanding monoliths as highly efficient multi-functional electrodes for highly compressible, and/or flexible energy conversion and storage devices. In our recent study, the fully interconnected fibrous freestanding membrane with abundant cobalt-nitrogen-carbon (Co-N-C) sites showed high tri-functional activity [30]. By excluding the supporting substrate, a large amount of active material is loaded into the 3D hierarchical porous monolith while minimizing the formation of embedded active sites. Due to the high aspect ratio of 1D fibrous structure, freestanding membrane could be self-assembled, while it was easily broken by the structural deformation. Therefore, ensuring high flexibility and/or compressibility of free-standing electrode remains a challenge. In contrast, the carbon monoliths derived from fibrous cellulose in biomass, i.e., miscanthus stem, have sufficient mechanical strength and high flexibility/compressibility as freestanding electrodes. The mechanical strength of the carbon monolith can be reinforced with a high tri-functional activity by the additional growth of carbon nanotube (CNT) bundles anchoring Co single atoms/nanoclusters, resulting in high catalytic activity even under severe structural deformation conditions. Typically, the optimal monolithic electrode exhibits highly efficient bi-functional activity for

alkaline water electrolysis, with an overpotential of 53 mV for HER and of 167 mV for OER at a current density of 10 mA cm^{-2} . In addition, a half-wave potential of $0.845 \text{ V}_{\text{RHE}}$ indicates a high ORR activity comparable to that of Pt/C. More importantly, the binder- and substrate-free freestanding monolithic electrodes lead to optimal performance in practical alkaline water electrolyzers and quasi-solid state ZABs. The water splitting system requires an applied potential of 1.56 V to generate a current density of 50 mA cm^{-2} , which surpasses the conventional electrodes with benchmarking noble-metal-based Pt/C and IrO_2 catalysts. In addition, the rechargeable ZAB with monolithic air cathode exhibits a high peak power density of 175.5 mW cm^{-2} , and an extremely small potential gap less than 0.4 V at 5 mA cm^{-2} . Finally, ZAB with monolithic air cathode exhibits reliable cycling performance without noticeable voltage gap changes under mechanical stresses accompanying structural deformations such as severe bending and compression, demonstrating the advantages of promising electrode designs for next-generation wearable energy devices.

2. Experimental section

2.1. Delignification of miscanthus to separate the inner- and outer-parts

3 g of dried miscanthus stems were firstly immersed into 60 mL of 3 M NaOH solution in a Teflon-lined stainless-steel autoclave. The delignification reaction was carried out at 120°C for 12 h in an electric oven, and naturally cooled down to room temperature. The pieces of miscanthus stems were washed thoroughly with de-ionized water by ultrasonication to separate the individual cellulose microfibrils in outer-part from the sponge-like monolithic inner-part. The separated cellulose microfibrils were collected by vacuum-filtration.

2.2. Preparation of freestanding monolithic catalyst electrodes

0.4 g of delignified miscanthus stems, regardless of inner- or outer-part, were immersed into a 60 mL methanol solution containing 1.5 g of cobalt (II) nitrate hexahydrate and 3.0 g of hexamethylenetetramine (HMTA). Then the solution was transferred to Teflon-lined stainless-steel autoclaves and heated at 120°C for 12 h. The resulting Co-coated miscanthus was washed repeatedly with methanol. The porous inner monolith coated with Co (denoted as inner@Co) was dried at room temperature, and the outer-microfibrils coated with Co were re-dispersed in methanolic solution ($\sim 1 \text{ mg mL}^{-1}$), and then collected as a freestanding monolith (denoted as outer@Co) by a vacuum filtration. The thickness of the monolith was controlled by the amount of the aqueous solution to obtain membrane-type and sponge-type monoliths. Then, as-prepared monoliths were placed in an alumina oxide boat, and another crucible containing 3 g of melamine was placed in the inlet-direction with a distance of 2 cm. Several pieces of inner@Co@CNTs and outer@Co@CNTs monoliths were prepared by an annealing process under argon flow at 700°C for 3 h with a ramping rate of 5°C min^{-1} . As the control groups, raw miscanthus stem, outer@Co, and inner@Co samples were converted to raw miscanthus@C, outer@Co@C, and inner@Co@C, respectively by an annealing process under the same conditions in the absence of melamine. The binder- and substrate-free monolithic carbon electrodes were cut to $1.5 \times 1.5 \text{ cm}^2$, and directly used without further treatment.

2.3. Preparation of conventional catalyst electrodes

The catalytic ink solution containing 20 mg of Pt/C (or IrO_2) catalysts, 3.8 mL isopropanol and 0.2 mL of 5 wt% Nafion solution was deposited onto commercial substrates (nickel foam for Pt/C, and carbon nanofiber paper for IrO_2) to prepare the conventional catalyst electrodes with a size of $5 \times 2 \text{ cm}^2$, resulting in a mass loading of 1 mg cm^{-2} .

2.4. Characteristics

Field emission scanning electron microscopy (FE-SEM, S-4800, Hitachi and Gemini 500, ZEISS), transmission electron microscopy (TEM, JEM-2100 F, JEOL) were carried out for the characterization of the nanostructure and morphologies of monolithic samples. The atomic-scale detailed nanoarchitecture was analyzed with aberration-corrected high-angle annular dark-field scanning transmission electron microscopy (HAADF-STEM, JEM ARM 200 F, JEOL). X-ray diffraction (XRD) patterns were obtained on X'Pert PRO diffractometer. The chemical states of samples were analyzed with X-ray photoelectron spectroscopy (XPS, K-ALPHA, ThermoFisher). Fourier-transform infrared (FT-IR) spectrums were obtained with Nicolet 6700, Thermo scientific. Raman spectrums were acquired by a laser Raman spectrophotometer (NRS-5100).

2.5. Electrochemical analysis

The bi-potentiostat workstation (ZIVE BP2C, WONATECK, Korea) was carried out to measure the electrochemical analysis. The HER and OER catalytic activity of samples were measured in three-electrode configuration with binder- and substrate-free monolithic electrodes directly as working electrodes, and graphitic rod or Pt coil as counter electrodes, and Hg/HgO (1 M NaOH) electrode as a reference electrode, respectively. All of the measured potentials were converted to the reversible hydrogen electrode (RHE) using the Nernst equation. Prior to LSV measurements for HER/OER evaluation, all of the samples were stabilized by 50 cycles of cyclic voltammetry at a scan rate of 100 mV s^{-1} in 1 M KOH electrolyte. LSV curves were obtained at 0.2 mV s^{-1} with 80% iR compensation to reduce the generation of non-faradaic current. The durability of monolithic electrodes was evaluated by the chronopotentiometric measurement in two-electrode configuration with a current density of 50 mA cm^{-2} . The ORR activity was evaluated in 0.1 M O_2 -saturated KOH electrolyte based on an rotating ring-disk electrode (RRDE). The catalyst ink solution was prepared by dispersing 10 mg of catalysts in 2 mL solvent containing 1.9 mL isopropanol, 100 μL of 5 wt % Nafion solution by ultrasonication. Then, 20 μL of the ink solution was dropped onto RRDE with the loading amount of $100 \mu\text{g cm}^{-2}$.

2.6. Fabrication of the quasi-solid-state ZABs

As-prepared binder- and substrate-free monolithic carbon electrodes were directly used as air cathodes without further treatment. The conventional air cathode was also prepared by coating the Pt/C catalyst ink solution onto gas diffusion layer (GDL, Avacarb-P75T) with a loading amount of 2 mg cm^{-2} . The quasi-solid-state ZABs were fabricated with the monolithic- or conventional-electrodes as air cathodes, with a zinc-foil as anode, and the mixture of polyvinylalcohol (PVA) and KOH as gel electrolyte. To prepare the PVA-KOH solution, 3 g of PVA (molecular weight of 146,000–186,000, 99% hydrolyzed) was dissolved in 30 mL of deionized water at 80°C with magnetic stirring to obtain a transparent solution. Then, 3 mL of 18 M KOH solution was slowly added into the solution and kept at 80°C for 90 min. The gel electrolyte was deposited on zinc foil, cooled naturally to room temperature, and then sandwiched with air cathodes. Typically, two types of monoliths with different thicknesses were various thicknesses were applied for membrane-type with 1.6 mm, and for sponge-type air cathodes with $\sim 1.2 \text{ cm}$. The thicknesses of zinc foil and PVA gel electrolyte were confirmed to be $\sim 0.28 \text{ mm}$, and $\sim 0.5 \text{ mm}$, respectively (Fig. S1a–d). The discharge/charge polarization curves and cycling test were examined at a current density of 5 or 10 mA cm^{-2} with the charge-discharge period of 5 min

3. Results and discussions

3.1. Preparation of monolithic electrodes derived from miscanthus stem

As illustrated in Fig. 1, the miscanthus stem has two different inner- and outer- lignocellulose parts consist of a porous rod-type inner part composed of tubular cells surrounded by an outer part of microfibrils. The miscanthus stem with the lignocellulose component was processed to selectively remove the lignin and hemicellulose to obtain the two different cellulose-based monoliths. Following a delignification process in 3 M NaOH solution at 120°C for 12 h, the outer-part was broken down into individual cellulose microfibrils, and at the same time was separated from the sponge-like porous inner-part cane. As shown in Fig. S2a, a black liquor containing the lignin was obtained after the delignification process, and the delignified miscanthus samples were precipitated. The cellulose microfibrils were naturally separated from the remaining rod-type monolith (Fig. S2b), and then uniformly dispersed in aqueous solution during an ultra-sonication process within 5 min. At this stage, each monolith was prepared along two routes; i) a porous rod-type monolith that retains its structure on the inner-part, ii) a self-assembled fibrous monolith using microfibrils separated from the outer-part. Thereafter, each delignified miscanthus sample was impregnated with cobalt species by a mild solution-based process in a methanol solution containing cobalt (II) nitrate hexahydrate and hexamethylenetetramine at 120°C for 12 h. Particularly for the second route to fabricate outer-part derived monoliths, the size and thickness, flexibility and compressibility could be controlled by varying the amount of methanol solution containing Co-coated cellulose microfibrils ($\sim 1 \text{ mg mL}^{-1}$). Last, the resulting monoliths were annealed at 700°C for 3 h in an argon atmosphere with melamine powder providing additional nitrogen and carbon elements. The cellulose component was converted into a freestanding carbon matrix, and at the same time, a number of carbon nanotubes (CNTs) were grown in-situ onto the surface of the monoliths. The synthesis method by combining metal nanoparticles and melamine powder during pyrolysis process has been extensively studied by many research groups to fabricate CNT-decorated transition metal-nitrogen-carbon (M-N-C) nanomaterials [30–32]. It is worth noting that our study mainly focuses on the freestanding electrode design, and the formation mechanism of the catalytic material, i.e., Co-N-C, is not significantly different from the pioneer studies, which confirmed the existence of atomic Co- N_x species with X-ray absorption spectroscopy [32]. In the presence of ammonia gas released from melamine or dicyandiamide powder [33] during the annealing process, metal nanoparticles are further dispersed into nanoclusters and single atoms to form coordination bonds with nitrogen [34,35]. Therefore, the improvement of the catalytic activity and/or mechanical properties such

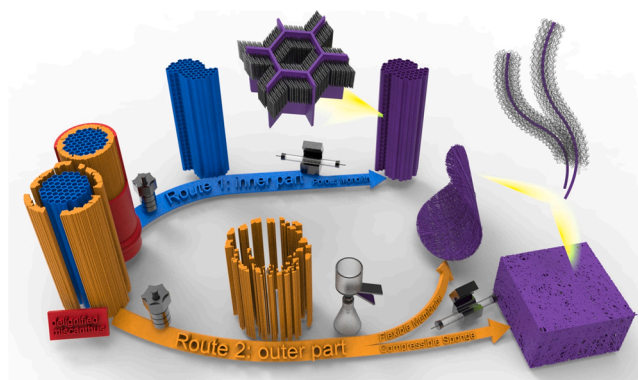


Fig. 1. Schematic illustration of miscanthus-derived monolithic carbon electrodes via two different synthetic strategies: i) porous carbon rod-type monoliths derived from the inner part, ii) highly flexible membrane-type and/or compressible sponge-type monoliths derived from outer part.

as high flexibility and compressibility of the catalytic electrode in this study mainly depends on rational electrode design. Benefiting from a fully-interconnected cellulose-derived carbon matrix, the resultant monolith was directly used as a binder- and substrate-free freestanding electrode without any further treatment. Photographs of each stage in the preparation of the inner-part derived porous monolith (corresponding sample is denoted as inner@Co@CNTs) or outer-part derived fibrous monolith (corresponding sample is denoted as outer@Co@CNTs) are shown in Figs. S3 and S4, respectively. The inner-part of raw miscanthus stem (Fig. S3a) retained well its original porous rod shape after successive delignification process (Fig. S3b), Co impregnation process (Fig. S3c), and following annealing process with melamine (Fig. S3d). On the other hand, the thickness of the outer-part derived fibrous monolith can be controlled by changing the amount of methanol solution containing cellulose microfibers coated with Co ($\sim 1 \text{ mg mL}^{-1}$) into the glass filtration funnel. In this way, the thickness of monolithic electrode was controlled from a few millimeters for the flexible membrane-type (Fig. S4a), to a few centimeters ($\sim 1.2 \text{ cm}$) for the compressible sponge-type monoliths (Fig. S4b). These cellulose-based monoliths were converted directly to carbon monoliths through an annealing process with a slight shrinkage (Fig. S4c, d), and the color changed from light brown to black. It is worth noting that more than 10 g of miscanthus can be processed in single-batch delignification process, and the size and shape of the monolithic sponges were dependent on the size/shape of glass funnel in the vacuum-filtration process, as well as the amount of solution (Fig. S5a, b). For comparison, miscanthus-derived monoliths in each synthesis step such as raw miscanthus (denoted as raw miscanthus@C), and delignified miscanthus (denoted as inner@C and outer@C), and Co-coated monoliths (denoted as inner@Co@C and outer@Co@C) were also pyrolyzed in the absence of melamine powder to obtain CNT-free carbonized monoliths. The structure and morphologies of carbonized monolith samples were analyzed by microscope images.

3.2. Morphology, structure, and chemical composition of monolithic carbon electrodes

The double-structure of the raw miscanthus stem (raw miscanthus@C) was observed by FE-SEM (Fig. S6a), comprised of the inner-part with tubular cells (Fig. S6b, c) and the outer-part with aligned fibrous structure (Fig. S6d–f). After delignification process, a porous surface of cylindrical rod composed of tubular cells was observed for inner@C sample (Fig. 2a–c). The presence of tubular cells in the rod-type monolith leads to a well-developed three-dimensional macroporous structure for inner@C. After hydrothermal reaction, plenty of Co nanoparticles were uniformly attached on the surface of inner@Co@C (Fig. 2d). In the presence of melamine, the original microporous structure is well-preserved for inner@Co@CNTs (Fig. 2e), and uniform growth of CNTs was observed in high-resolution SEM images in Fig. 2f–h. The growth of CNTs on both sides of the tubular cell wall was also confirmed in Fig. S7a–d. As shown in TEM images of Fig. 2i and j, numerous CNTs are anchored to the surface of the cobalt-embedded carbon matrix. HR-TEM image in Fig. 2k shows the presence of Co nanoclusters at the edge of the CNT wall as well as metallic nanoparticles encapsulated by the graphene wall at the tip of the CNT. In the inset image of Fig. 2k, a lattice fringe of 0.205 nm was observed indexed to the (111) facet of metallic cobalt. STEM images and the corresponding elemental mapping images of inner@Co@CNTs (Fig. 2l) reveal the presence of nitrogen, carbon, and cobalt elements. On the other hands, the individual cellulose microfibers from the outer-part can be reassembled into a freestanding monolith with high interconnectivity (Fig. 3a, b). The individual microfibers, with an average diameter of several micrometers, are composed of entangled nanofibers (Fig. 3c). Furthermore, a rough and porous surface was observed in Fig. 3d, compared to the smooth surface of the tubular cell wall (Fig. S8a–c). Therefore, Co nanomaterials with a nanoneedle-like shape are densely loaded on the surface of microfibers (Fig. S9a, b), and converted into

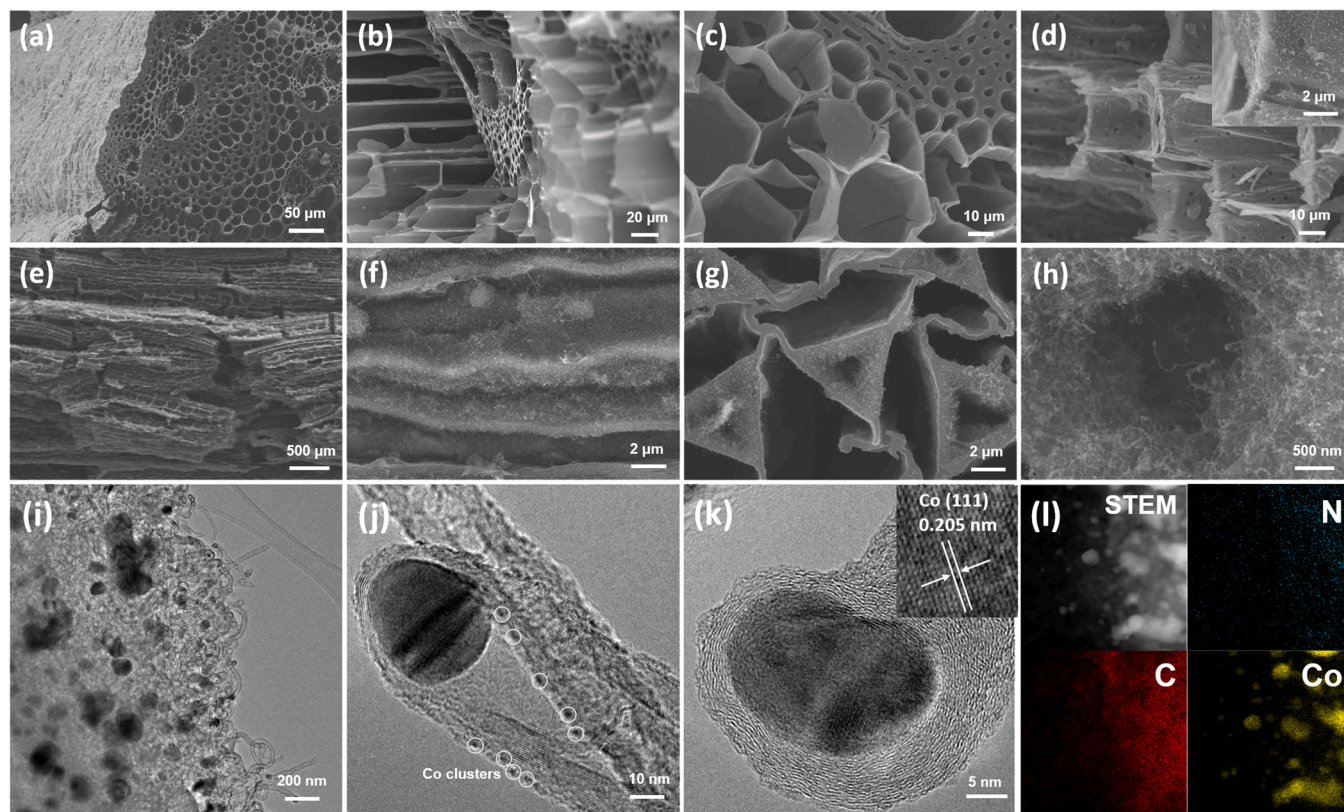


Fig. 2. SEM images of (a)–(c) raw miscanthus@C, (d) inner@Co@C, (e)–(h) inner@Co@CNTs. (i) TEM and (j,k) HR-TEM (inset in (k): lattice fringe of metallic Co nanoparticle), (l) STEM image and corresponding N, C, Co elemental mapping images of inner@Co@CNTs.

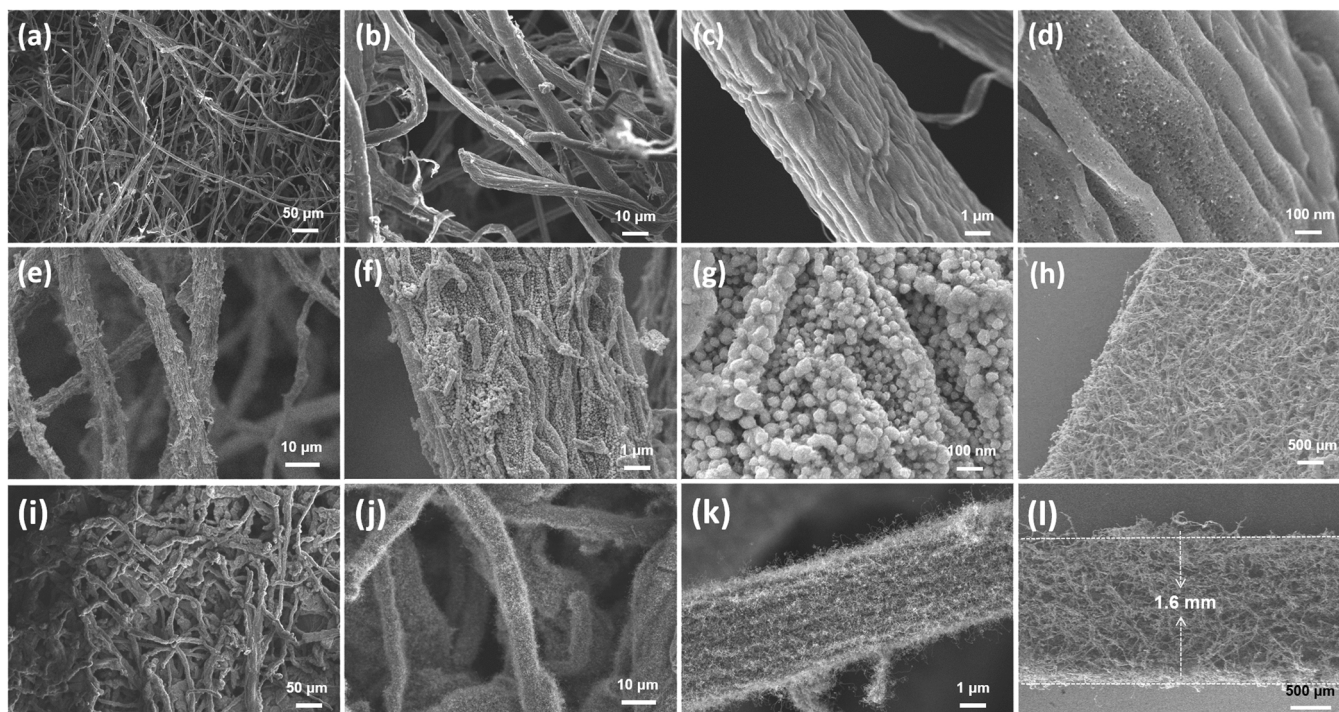


Fig. 3. Top-view SEM images of (a)-(d) outer@C, (e)-(g) outer@Co@C, (h)-(k) outer@Co@CNTs. (l) Cross-sectional SEM image of outer@Co@CNTs membrane with an average height of 1.6 mm.

uniform Co nanoparticles after annealing process (Fig. 3f, g). The highly interconnected fibrous network generates numerous macropores (Fig. 3h, i), and the fibrous matrix is uniformly covered with bundles of CNTs (Fig. 3j, k). The cross-sectional SEM image in Fig. 3l shows a

sponge-like matrix composed of 1D cellulose-derived carbon microfibers, and the average thickness of the membrane-type carbon monolith from 100 mL solution ($\sim 1 \text{ mg mL}^{-1}$) was found to be $\sim 1.6 \text{ mm}$, with a mass loading of $\sim 21 \text{ mg cm}^{-2}$. The mass loading of Co in

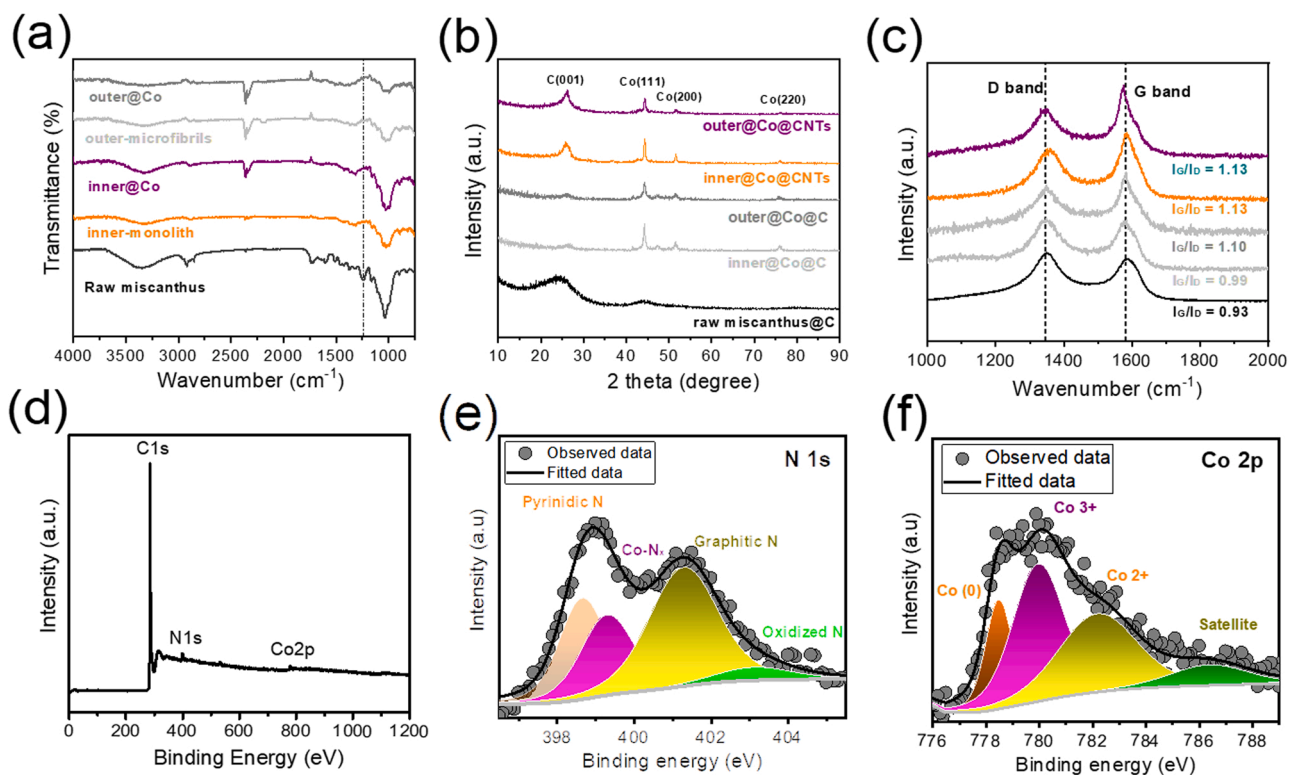


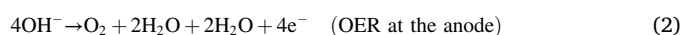
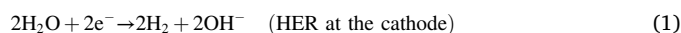
Fig. 4. (a) FT-IR spectra of raw miscanthus, and inner- and outer-part of miscanthus samples after delignification and/or Co incorporation processes, respectively. (b) XRD patterns, (c) Raman spectra of raw miscanthus@C, inner@Co@C, inner@Co@CNTs, outer@Co@C, and outer@Co@CNTs. (d) XPS survey spectrum, and fine (e) N1s, (f) Co2p XPS spectra of outer@Co@CNTs.

inner@Co@CNTs and outer@Co@CNTs monolithic electrode was also calculated by thermo-gravimetric analysis (TGA) results to be 1.54, and 2.95 wt%, respectively (Fig. S10). The surface of cellulose-derived carbon microfibers anchored with CNTs (Fig. S11a), and the presence of Co nanoclusters and encapsulated nanoparticles at the tip of CNTs (Fig. S11b) were also observed in the HR-TEM images. In the presence of melamine powder during the annealing process, it decomposed to initiate further growth of CNTs for inner@Co@CNTs and outer@Co@CNTs. More specifically, at temperatures above 350 °C, melamine decomposes to produce ammonia gas, which can etch the Co solid precursor and disperse it into smaller Co nanoclusters/single atoms [36, 37]. The decomposed melamine also provides carbon and nitrogen elements to promote the growth of CNTs [38] encapsulating metallic Co nanoparticles, and simultaneously generates a coordination between Co and N in carbon matrix as abundant Co-N_x moieties. To verify the presence of atomic Co-N_x active sites in carbon monoliths, the carbon matrix of inner@Co@CNTs (Fig. S12a) and the graphitic walls of an as-grown carbon nanotube in outer@Co@CNTs (Fig. S12c) were observed with atomic-scale HAADF-STEM images (Fig. S12b, d). The presence of atomic Co sites can be observed both in the carbon matrix and in the graphene layers of CNTs, as indicated as white circles. The formation of a rough and hydrophilic surface on the miscanthus stem is the key factor affecting the deposition of the cobalt nanoparticles and the subsequent growth of CNTs. In FT-IR spectrum of the raw miscanthus sample (Fig. 4a), the peaks of methoxy groups located at 1266 cm⁻¹ [39], and of CH₂ and CH₃ at 1460 cm⁻¹, and of C=C and C=O in aromatic rings at 1600 cm⁻¹ were observed, indicating the presence of the lignin component. Those peaks were greatly reduced after the delignification process, while a broad peak located at 3360 cm⁻¹ of the -OH groups stretching vibration, and of C-H stretching vibration at 2881 cm⁻¹, and of -CH₂ and CH bonds at 1425, and of C-O-C glycosidic band stretching vibration at 1024 cm⁻¹ remained, indicating that the cellulose component was preserved [40]. It is worth noting that at high temperatures above 150 °C, the delignification process also dissolves the cellulosic component, leading to low production yields. Thin-film X-ray diffraction (XRD) patterns of the carbonized monolithic samples are shown in Fig. 4b. The broad peak at 26°, corresponding (002) plane of graphitic carbon for carbonized raw miscanthus@C was sharpened for inner@Co@C and inner@Co@CNTs due to the formation of Co-catalyzed graphene walls. Similar trends were observed for outer@Co@C and outer@Co@CNTs. In addition, the diffraction peaks at 44°, 51°, and 76° indexed to metallic cobalt (JCPDS 15-0806) were observed in all of the Co-loaded samples. Recently, it has been proven that the presence of Co/CoO_x heterostructures in Co nanoparticles significantly enhances ORR activity [41–44]. Although some peaks corresponding to the Co₃O₄ phase in outer@Co@CNTs were observed by the Raman spectroscopy (Fig. S13), the presence of Co₃O₄ was not confirmed in the XRD patterns and HR-TEM images of Co nanoparticles. Therefore, it can be seen that most of Co₃O₄ phase was reduced to metallic Co phase due to the presence of abundant carbon sources during the annealing process. As shown in Raman spectrum in Fig. 4c, the relative peak intensity of I_G/I_D in miscanthus@C was 0.93, and increased to 0.99 and 1.10 for inner@Co@C and outer@Co@C, respectively. Those values were further improved to 1.13 for both inner@Co@CNTs and outer@Co@CNTs, indicating the high graphitic degree attributed to Co-catalyzed formation of graphene layers of the CNTs. The chemical states and electronic structures of the monoliths were analyzed by XPS analysis. The survey spectrum of outer@Co@CNTs (Fig. 4d) confirmed the presence of cobalt and nitrogen elements with 3.2 wt% for cobalt, and 7.8 wt% for nitrogen. The high-resolution N1s XPS spectrum (Fig. 4e), was deconvoluted to four peaks located at 398.7, 399.3, 401.3, and 403.3 eV, corresponding to pyridinic N, Co-N_x, graphitic N, and oxidized N, respectively [22]. In Co 2p spectrum in Fig. 4f, three peaks located at 778.2, 780.6, 782.2 eV were observed, assigned to zero-valence state metallic cobalt, Co³⁺, and Co²⁺, respectively [45], with a broad satellite peak at 786.7 eV. In the

absence of melamine, the annealed outer@Co@C sample showed no significant nitrogen signal in the survey (Fig. S14a), and N1s (Fig. S14b) spectrums. Furthermore, the Co 2p spectrum of outer@Co@C (Fig. S14c) showed no peak assigned to metallic Co, indicating the role of melamine in reducing Co by providing a carbon and nitrogen source during the carbonization process. The XPS survey spectrum of inner@Co@CNTs in Fig. S15a also confirmed the existence of nitrogen and cobalt species, while the ratio of cobalt and nitrogen species was 2.2 and 5.6 wt%, relatively lower than the values of outer@Co@CNTs. The high resolution N1s (Fig. S15b) and Co2p (Fig. S15c) spectrums showed the chemical states similar to those of outer@Co@CNTs.

3.3. Multi-functional activity and overall water splitting with monolithic carbon electrodes

In our study, the water electrolysis system is based on HER and OER, and operated in alkaline liquid electrolyte. The alkaline water splitting consists of two half-reactions of HER and OER as follows,



Firstly, the bi-functional catalytic activities toward HER and OER for alkaline water electrolysis were investigated. The i-v curves of raw miscanthus@C, inner@Co@CNTs, outer@Co@CNTs were obtained by linear scanning voltammetry (LSV) in 1 M KOH electrolyte toward HER. As the control samples, the conventional electrodes with benchmarking Pt/C or IrO₂ catalysts were prepared by coating of powdery catalyst on commercial substrates (nickel foam for Pt/C, and carbon nanofiber paper for IrO₂). As shown in Fig. 5a and the inset images, raw miscanthus@C exhibits an overpotential value (η₁₀) of 268 mV at a current density of 10 mA cm⁻², indicating relatively poor HER activity. Upon the introduction of cobalt nanoparticles onto carbon matrix, outer@Co@C shows a much improved overpotential value (η₁₀) of 119 mV. This η₁₀ value is greatly reduced for inner@Co@CNTs and outer@Co@CNTs to 82 and 53 mV, respectively, slightly larger than that of Pt/C (η₁₀ = 28 mV), indicating excellent HER activity. Benefiting from the monolithic characteristics with abundant accessible active sites, those miscanthus-derived electrodes shows the advantages particularly at the high current densities such as j = 100 mA cm⁻² with the small overpotential values (η₁₀₀ = 189 mV for inner@Co@CNTs and η₁₀₀ = 182 mV for outer@Co@CNTs), similar to that of Pt/C (η₁₀₀ = 192 mV) electrode. Considering that most of cobalt-nitrogen-carbon (Co-N-C) catalysts reported so far showed much inferior HER activity compared to Pt/C catalysts in the "conventional" electrode configuration [46], the superior HER activity in this study demonstrates the advantages of monolithic electrodes with abundant accessible active sites. As shown in Fig. 5b, the Tafel slope value of outer@Co@CNTs is smaller (41.75 mV dec⁻¹) than those of raw miscanthus@C (150.2 mV dec⁻¹), outer@Co@C (78.78 mV dec⁻¹), and inner@Co@CNTs (69.76 mV dec⁻¹). This indicates faster hydrogen evolution reaction kinetics which follow the Volmer-Heyrovsky mechanism [47]. Next, the OER polarization curves of as-prepared monolithic electrodes and IrO₂ catalyst were illustrated in Fig. 5c. The outer@Co@CNTs sample afforded the smallest overpotential value (η₁₀ = 167 mV, and η₁₀₀ = 360 mV) compared to miscanthus@C (η₁₀ = 400 mV), outer@Co@C (η₁₀ = 320 mV and η₁₀₀ = 395 mV), inner-Co@CNTs (η₁₀ = 254 mV and η₁₀₀ = 376 mV), and IrO₂ (η₁₀ = 331 mV and η₁₀₀ = 422 mV). Fig. 5d shows the corresponding Tafel slope of outer-Co@CNTs with a smaller value (98.41 mV dec⁻¹) compared to those of raw miscanthus@C (249.24 mV dec⁻¹) or IrO₂ (124.47 mV dec⁻¹), revealing the favorable reaction kinetics for OER. Electrochemical impedance spectroscopy (EIS) measurements were carried out to investigate the charge transfer kinetics of the electrochemical reaction processes involved in both HER (Fig. S16a) and OER (Fig. S16b). The smallest charge transfer resistance (R_{ct}) value is obtained for outer@Co@CNTs, which implies the accelerated reaction

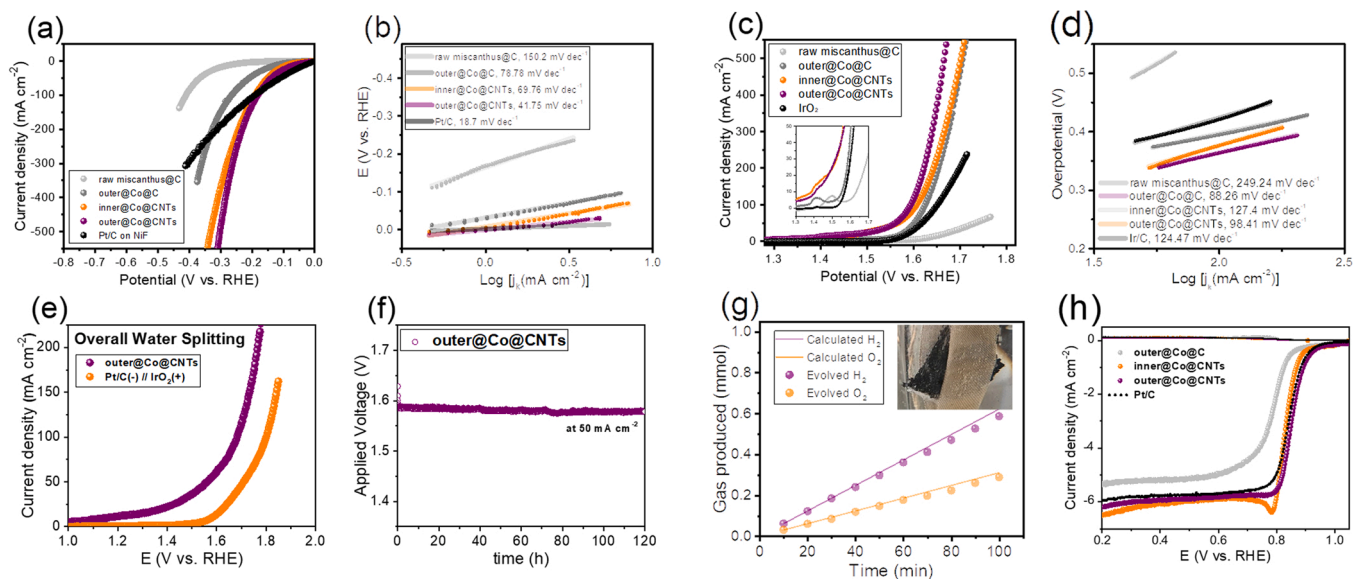


Fig. 5. (a) LSV curves of miscanthus-derived monolithic electrodes and Pt/C in 1 M KOH electrolyte toward HER at a scan rate of 0.2 mV s⁻¹. (b) Tafel plots derived from panel (a). (c) LSV curves toward OER, and (d) corresponding Tafel plots. (e) LSV curves of alkaline water splitting with two outer@Co@CNTs or Pt/C for HER and IrO₂ for OER, (f) chronoamperometric test of alkaline water electrolyzer at $j = 50 \text{ mA cm}^{-2}$, and the inset photograph image of outer@Co@CNTs during alkaline water splitting. (g) The theoretical, and experimental gas evolution of oxygen and hydrogen at a current density of 20 mA cm^{-2} , and the inset photograph image of outer@Co@CNTs during alkaline water splitting. (h) LSV curves of outer@Co@C, inner@Co@CNTs, outer@Co@CNTs, and Pt/C catalysts on RRDE in O₂-saturated 0.1 M KOH electrolyte at a scan rate of 1 mV s⁻¹ and at a rotating rate of 1600 rpm.

kinetics and reduced internal and/or interfacial resistances within monolithic electrode. The better catalytic activity and smaller R_{ct} values of outer@Co@CNTs compared to inner@Co@CNTs can be attributed to the 1D fibrous structure of outer@Co@CNTs, which leads to favorable electrical conductivity compared to the porous structure of inner@Co@CNTs. Furthermore, the higher Co content in outer@Co@CNTs compared to inner@Co@CNTs, confirmed in TGA result, indicates that the formation of a large number of deposited Co nanoparticles for growth of CNTs with abundant Co-N-C active sites. The overall water splitting in the 1 M KOH electrolyte was evaluated using two identical freestanding outer@Co@CNTs monoliths, as shown in Fig. 5e. The applied potential of the alkaline water electrolyzer in 1 M KOH was 1.45 V at a current density of 10 mA cm^{-2} , which was one of the best performances of the two bi-functional catalytic electrodes, surpassing that of Pt/C(-) and IrO₂(+). This potential value for alkaline water electrolyzer is one of the highest bi-functional activity including the recently reported self-supporting electrodes [48–52] (Table S1). The durability of this hydrogen production system was evaluated by chronopotentiometric test with a current density of 50 mA cm^{-2} , and there was no significant change in an applied potential of about 1.56 V for more than 120 h. The stoichiometric molar ratio of hydrogen and oxygen evolution was confirmed to be 2:1 based on gas chromatography (Fig. 5g). The ORR activity of the miscanthus-derived samples was also investigated in rotating ring-disk electrode (RRDE) experiments in O₂-saturated 0.1 M KOH electrolyte. As shown in the i-v curves of the LSV measurements in Fig. 5h, outer@Co@CNTs and inner@Co@CNTs exhibited similar half-wave potentials of 0.845 and 0.832 V_{RHE}, which is close to that of Pt/C (0.835 V_{RHE}), and superior to that of outer@Co@C (0.785 V_{RHE}). The lower Tafel slope of outer@Co@CNTs of 77.63 mV dec⁻¹ compared to those of outer@Co@C (99.91 mV dec⁻¹), inner@Co@CNTs (77.63 mV dec⁻¹), and Pt/C (94.23 mV dec⁻¹) was confirmed in Tafel plots (Fig. S17), indicating the favorable ORR kinetics. The hydrogen peroxide yield and electron transfer number of the samples were also calculated from the current densities of the ring and disk electrodes, as illustrated in Fig. S18. The electron transfer number of inner@Co@CNTs and outer@Co@CNTs samples is ~ 3.9 , very close to that of Pt/C, indicating the direct 4-electron pathway in ORR. Similarly, the hydrogen peroxide yield of inner@Co@CNTs, outer@Co@CNTs,

and Pt/C is below 9% over a potential range from 0.2 to 1.0 V_{RHE}, while that of outer@Co@C possesses relatively higher H₂O₂ yield of up to 21%. Note that the recorded ORR activity is based on RRDE prepared by disassembling the monolithic electrode and applying a powder catalyst on top of the glassy carbon electrode. Therefore, the practical electronic devices utilizing the monolithic electrode directly are expected to have further improved ORR catalytic activity. In the previously reported literatures, some cobalt-nitrogen-carbon (Co-N-C) have been used as catalyst materials with tri-functional activity including the self-supporting electrodes based on carbon cloth [22], graphene aerogel [37], cobalt foil [53], and electrospun carbon nanofibers [24,54]. Nevertheless, the optimal catalytic activity of this study surpasses the state-of-the-art multi-functional catalysts [55–59] as summarized in Table S2, which can be explained by the advantages of freestanding monolithic electrode with rational 3D hierarchical structure. In terms of interfacial engineering, the accessibility of reactive molecules to the active site is enhanced by the hierarchical porous structure of the 3D monolithic electrode, effectively suppressing the interfacial resistance by inducing high electron and mass transfer through the tightly and fully interconnected nanonetwork. As a result, the monolithic electrode design dramatically reduces interfacial energy losses caused by conventional electrode structures, simultaneously increasing initial performance and durability in both water electrolyzers and zinc-air batteries. Moreover, the interconnectivity of the entangled carbon microfibers constituting the monolithic electrode can be further improved by surface growth of CNTs, which further improves the mechanical properties of the electrode. Consequently, the fibrous monolith can be expected to have high enough flexibility and compressibility as well as high enough mechanical strength as a freestanding electrode due to the highly interconnected 1D carbon network.

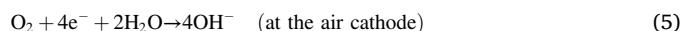
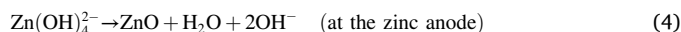
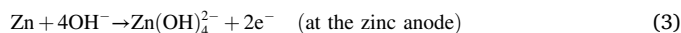
Recently, it has been proven that cobalt single atoms coordinated with nitrogen (Co-N_x) have appropriate free energies for the reaction intermediates of HER, OER and ORR by density-function theory (DFT) calculations, and their multifunctional activity has been demonstrated experimentally [24,60]. Despite the high theoretical multi-functional activity of atomic Co-N_x sites, the experimental activity exhibited poor activity particularly in the multielectron reaction process such as OER, mainly due to their low electrical conductivity [61]. Therefore, the

coexistence of nanoparticles and nanoclusters can work as competitive active center to single atomic Co-N_x sites, which simultaneously promotes the dissociation of water molecules [62] in alkaline electrolyte, and/or improves the electronic conductivity of the bulk electrodes, ensuring high multi-functional catalytic activity at the same time. Thus, the co-existence of atomic Co-N_x along with metallic Co nanoclusters and nanoparticles leads to the excellent tri-functional activity in in monolithic electrodes with relatively high mass loading of active materials. To investigate the individual and synergistical roles of Co-based active sites in multi-functional activity, two additional experiments were conducted for outer@Co@CNTs sample. Firstly, the catalytic activity of outer@Co@CNTs were evaluated after the removal of exposed Co nanoparticles (NPs) by acid-etching process with 6 M HCl solution at 80 °C for 12 h. Interestingly, the HER (Fig. S19a) activity of outer@Co@CNTs showed no significant change in catalytic activity, while OER activity was reduced (Fig. S19b). In addition, ORR activity also showed no meaningful change in terms of its half-wave potential (Fig. S19c). In the second experiment, the HER activity of outer@Co@CNTs were analyzed in 1 M KOH electrolytes with thiocyanate ion (SCN⁻). By the introduction of SCN⁻ ions, both HER (Fig. S20a) and OER (Fig. S20b) activities of outer@Co@CNTs were drastically decreased due to the poisoning of metal-N_x sites by SCN⁻ ions [62,63]. However, ORR activity of outer@Co@CNTs (Fig. S20c) showed no significant change, probably due to the competitive adsorption of hydroxyl and SCN⁻ on Co-N_x sites [64]. Based on the results of two experiments, the co-existence of Co single atoms and Co NPs particularly contributed to OER activity, whereas the primary active sites of HER and ORR could be Co-N_x atomic sites.

3.4. Performances of highly flexible, and/or compressible quasi-solid state ZABs with monolithic carbon air cathodes

In our study, ZABs system at air cathode is based on OER and ORR, and operated in quasi solid-state KOH-PVA gel electrolyte. The main active species in the electrochemical reaction is hydroxide ions (OH⁻), and both the KOH solution and the PVA polymer matrix contribute to the transport of OH⁻ [65]. Therefore, the OH⁻ transport mechanism of KOH-PVA gel electrolyte is similar to that of alkaline aqueous

electrolyte. During the discharge process, the metallic zinc anode is oxidized and reacts with OH⁻ ions to produce zinc intermediate ions and zinc oxide. At the air cathode, oxygen gas molecules can diffuse into the porous 3D carbon matrix and the ORR process occurs in the three-phase reaction region between the gas-liquid (gel)-solid interfaces. Therefore, the relevant reactions are as follows,



In our system, PVA-KOH gel electrolyte offers high mechanical properties such as flexibility and/or compressibility, unlike the liquid-phase electrolyte system. Lastly, the feasibility of binder- and substrate-free outer@Co@CNTs monoliths as air cathodes for highly flexible, and/or compressible gel-type zinc-air batteries (ZABs) was evaluated. Two types of monoliths with different thicknesses were used without any further treatment, either of a highly flexible membrane-type or a compressible 3D carbon sponge-type ZABs. As illustrated in Fig. 6a, the flexible ZABs were fabricated using the membrane-type outer@Co@CNTs as air cathodes, and zinc foil as the anode, with a gel-type polyvinylalcohol (PVA) electrolyte with KOH. Nickel foam was used as the current collector, and notably, the cyclic performance of the ZAB was not affected by the presence of nickel foam. For comparison, a conventional air cathode was also prepared by deposition of benchmarking Pt/C catalyst layer on carbon nanofiber paper with a mass loading of ~ 2 mg cm⁻². As shown in Fig. 6b, the peak power density of ZAB with outer@Co@CNTs air cathode was 175.5 mW cm⁻², surpassing that of conventional Pt/C air cathode (68.7 mW cm⁻²). Particularly for charging polarization curve, Pt/C showed drastically increased applied voltage compared to outer@Co@CNTs monolith due to its poor OER activity. Therefore, ZAB with monolithic electrode exhibited a narrow average charge-discharge voltage gap in overall current range exceeding 100 mA cm⁻². This flexible membrane-type air cathode holds a large amount of active material (~ 21 mg cm⁻²), while minimizing inaccessible active sites due to the monolithic features. The significant

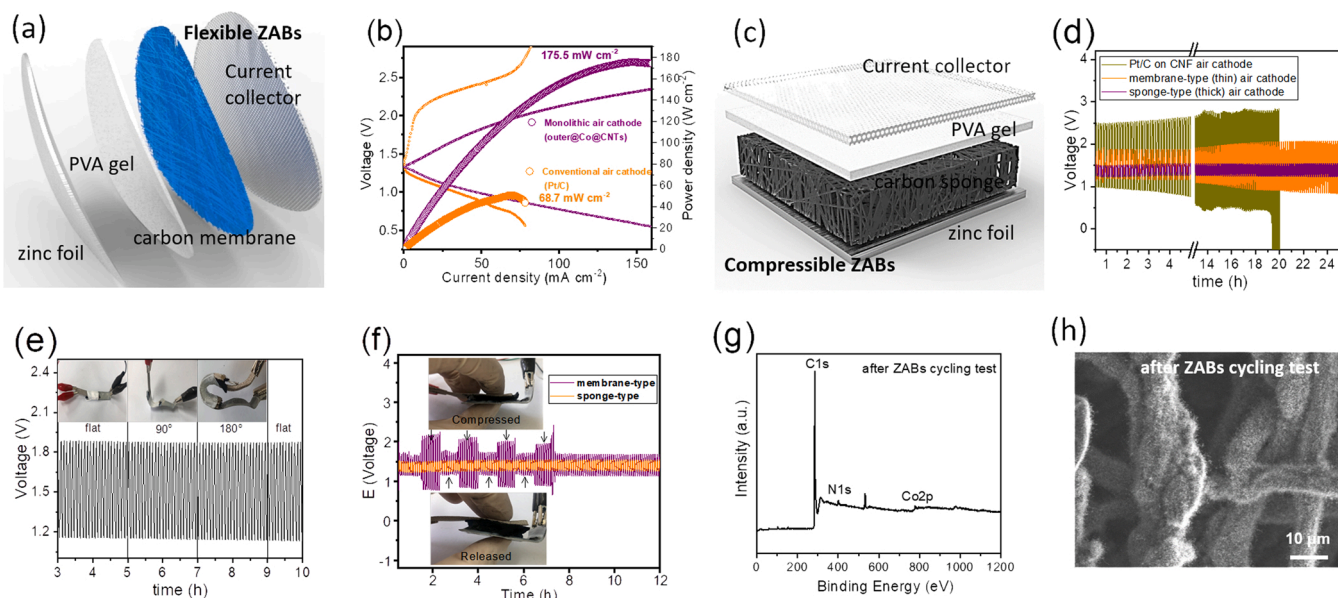


Fig. 6. (a) Schematic illustration of the fabrication of solid-state, flexible ZABs with membrane-type outer@Co@CNTs air cathode. (b) Charge and discharge polarization and power density curves of ZABs with monolithic air cathode of outer@Co@CNTs, and with a conventional air cathode of Pt/C loaded on CNF paper. (c) The structure of compressible ZABs with outer@Co@CNTs carbon sponge monolith. (d) Galvanostatic charge-discharge profiles of ZABs. (e) Cyclic performance of flexible ZABs with membrane-type air cathode under different bending angles. (f) Cyclic performances of compressible ZABs with sponge-type monolithic air cathode under compression and releasing state. (g) XPS survey spectrum and (h) SEM image of outer@Co@CNTs after cycling test.

improvement in actual ZAB performance compared to the conventional Pt/C air cathode ($\sim 2 \text{ mg cm}^{-2}$) may be due to the high mass loading of active materials evenly located over the entire monolithic electrode. The hierarchical porous carbon matrix generates a 3D reaction domain for gas-liquid-solid interface towards OER and ORR. In addition, highly compressible ZABs were also fabricated with monolithic carbon sponge air cathode (Fig. 6c), prepared by the vacuum filtration of a larger amount of cellulose microfibrils solution, and then used as the air electrode of gel-type, highly compressible ZABs. The membrane-type carbon monolith showed good flexibility under highly bending conditions (Fig. S21), while carbon sponge monolith showed good recovery after heavily compressed deformation condition (Fig. S22). As shown in Fig. 6d, the small voltage gaps between charge-discharge potentials of the ZABs with monolithic air cathodes are confirmed ($1.53\text{--}1.26 \text{ V} = 0.27 \text{ V}$ for sponge-type, and $1.82\text{--}1.17 = 0.65 \text{ V}$ for membrane-type) at a current density of 5 mA cm^{-2} , which is smaller than that of conventional Pt/C ($2.5\text{--}0.97 \text{ V} = 1.53 \text{ V}$) and recently reported ZABs [23,25,66–68] (Table S3). Thus, the calculated round-trip efficiency of the optimal ZABs was $\sim 82\%$, which was well-preserved to $\sim 81\%$ after the operation time for 24 h. On the other hands, ZABs with Pt/C air cathode exhibited the initial voltage gap with $\sim 1.53 \text{ V}$ ($2.5\text{--}0.97 \text{ V}$), which was steadily increased as the number of cycles is increased. The charge-discharge polarization curves of flexible membrane-type ZABs were not significantly changed, even with bending angles of 45° , 90° , and 180° (Fig. 6e), indicating its high flexibility due to the interconnected micro-fibrous network. In addition, the voltage gap of this ZAB with relatively thin membrane-type air cathode slightly increases in the compressed state to half its initial volume, and can then recover again when the pressure is released. By applying relatively thick carbon sponge ($\sim 1.2 \text{ cm}$) as air cathodes, no significant change in the voltage gap was observed even in the compressed state. The initial voltage gap less than 0.3 V of sponge-type ZABs was well-preserved after repeated compression and release tests. The galvanostatic charge-discharge curves of membrane- and sponge-type ZABs were also illustrated in Fig. S23a with the current densities at 1, 2, 5, and 10 mA cm^{-2} . Again, sponge-type ZABs showed smaller voltage gap values compared to those of membrane-type ZABs. The cyclic performance of ZABs at a current density of 10 mA cm^{-2} showed good initial voltage gap less than 0.4 V , and successfully cycled over 8 h (Fig. S23b). To investigate the thickness of sponge-type air cathodes on the performances of ZABs, different air electrodes of outer@Co@CNTs with the thickness of ~ 0.4 , ~ 1.2 , and $\sim 1.6 \text{ cm}$ were prepared, as shown in Fig. S24a–c. However, the cyclic performances of three different sponge-type ZABs showed no significant change in their initial voltage gaps (Fig. S25), maybe due to the limited diffusion of PVA-KOH electrolyte into carbon monolith, considering the millimeter-scale thickness of PVA-KOH gel electrolyte. The chemical states of outer@Co@CNTs after ZABs cycling were analyzed by XPS. There was also no significant change found in the chemical compositions in the survey spectrum (Fig. 6g), high resolution N1s (Fig. S26a) and Co2p (Fig. S26b) spectra except for the increased peak intensity of oxygen. In particular, the oxidizing conditions of the charging process led to the oxidation and partial decomposition of carbon. SEM images of monolithic air electrode after cycling test under the deformation conditions showed no significant change in its interconnected carbon network (Fig. S27a–c), as well as the detailed 1D fibrous structure decorated with a number of CNTs (Fig. 6h). The high durability of the monolithic electrodes can be attributed to the micro-scale highly graphitic carbon matrix and its initial high catalytic activity, which leads to the minimized applied overpotential.

4. Conclusions

To summarize, 3D freestanding monolithic electrodes with controllable flexibility and/or compressibility were synthesized from the double inner- and outer-structures of miscanthus stem. The delignification

process onto miscanthus stem led to the separation of individual cellulose microfibrils in outer-part from the remaining inner-part, and each separated outer- and inner-part convert to different types of monoliths. Uniformly dispersed Co nanoparticles, nanoclusters and single atoms coexist hierarchically on porous carbon, which greatly reduces the applied overpotential of multiple electrochemical reactions, leading to superior initial catalytic activity and long-term durability. Benefiting from the additional growth of CNTs reinforcing the 3D carbon network, the monolithic electrode supports itself without a supporting substrate and exhibits a good recovery from structural deformations such as bending and compression states. Freestanding monolithic electrodes with the abundant active sites opens up the potential for direct electrode application for alkaline water electrolyzers and solid-state zinc-air batteries. Therefore, the alkaline water electrolyzer with monolithic electrodes efficiently generated hydrogen at a current density of 50 mA cm^{-2} with a potential of 1.56 V for over 120 h. In addition, the semi-solid-state zinc-air cell (ZAB) exhibits low charge-discharge overpotential with an outstanding peak power density of 175.5 mW cm^{-2} and a remarkably small voltage gap (ΔV) of less than 0.4 V at 5 mA cm^{-2} . In particular, the flexible and compressible ZABs can operate stably maintaining its small voltage gap even under structurally deformed conditions such as bending and compressing. In conclusion, this study to produce a multi-functional carbon monoliths from wasted bio-resources would provide a new aspect for the rational design for binder- and substrate-free monolithic electrode and its direct application to next-generation wearable electronic devices.

CRedit authorship contribution statement

Hong Jin Son: Conceptualization, Investigation, Writing – original draft. **Ye Rim Cho:** Investigation, Writing – original draft. **Ye-Eun Park:** Investigation. **Sung Hoon Ahn:** Conceptualization, Writing – review & editing, Supervision, Project administration, Funding acquisition.

Declaration of Competing Interest

The authors declare that they have no known competing financial interests or personal relationships that could have appeared to influence the work reported in this paper.

Acknowledgments

This work was supported by the National Research Foundation of Korea (NRF) grant funded by the Korea government (MSIT) (Nos. NRF-2018R1C1B6005009 and NRF-2021R1C1C1012676).

Appendix A. Supplementary material

Supplementary data associated with this article can be found in the online version at [doi:10.1016/j.apcatb.2021.120977](https://doi.org/10.1016/j.apcatb.2021.120977).

References

- [1] M. Borghei, J. Lehtonen, L. Liu, O.J. Rojas, Advanced biomass-derived electrocatalysts for the oxygen reduction reaction, *Adv. Mater.* 30 (2018), 1703691, <https://doi.org/10.1002/adma.201703691>.
- [2] C.B. Jin, J.W. Nai, O.W. Sheng, H.D. Yuan, W.K. Zhang, X.Y. Tao, X.W. Lou, Biomass-based materials for green lithium secondary batteries, *Energy Environ. Sci.* 14 (2021) 1326–1379, <https://doi.org/10.1039/d0ee02848g>.
- [3] W.J. Liu, H. Jiang, H.Q. Yu, Emerging applications of biochar-based materials for energy storage and conversion, *Energy Environ. Sci.* 12 (2019) 1751–1779, <https://doi.org/10.1039/c9ee00206e>.
- [4] C.C. Qin, H. Wang, X.Z. Yuan, T. Xiong, J.J. Zhang, J. Zhang, Understanding structure-performance correlation of biochar materials in environmental remediation and electrochemical devices, *Chem. Eng. J.* 382 (2020), 122977, <https://doi.org/10.1016/j.cej.2019.122977>.
- [5] C. Wang, N.-H. Xie, Y. Zhang, Z. Huang, K. Xia, H. Wang, S. Guo, B.-Q. Xu, Y. Zhang, Silk-derived highly active oxygen electrocatalysts for flexible and rechargeable Zn-air batteries, *Chem. Mater.* 31 (2019) 1023–1029, <https://doi.org/10.1021/acs.chemmater.8b04572>.

- [6] T. Iwazaki, R. Obinata, W. Sugimoto, Y. Takasu, High oxygen-reduction activity of silk-derived activated carbon, *Electrochem. Commun.* 11 (2009) 376–378, <https://doi.org/10.1016/j.elecom.2008.11.045>.
- [7] Z.P. Zhang, S.X. Yang, H.Y. Li, Y.X. Zan, X.Y. Li, Y. Zhu, M.L. Dou, F. Wang, Sustainable carbonaceous materials derived from biomass as metal-free electrocatalysts, *Adv. Mater.* 31 (2019), 1805718, <https://doi.org/10.1002/adma.201805718>.
- [8] C.J. Lei, S.L. Lyu, J.C. Si, B. Yang, Z.J. Li, L.C. Lei, Z.H. Wen, G. Wu, Y. Hou, Nanostructured carbon based heterogeneous electrocatalysts for oxygen evolution reaction in alkaline media, *ChemCatChem* 11 (2019) 5855–5874, <https://doi.org/10.1002/cctc.201901707>.
- [9] Y.Z. Zhu, J. Sokolowski, X.C. Song, Y.H. He, Y. Mei, G. Wu, Engineering local coordination environments of atomically dispersed and heteroatom-coordinated single metal site electrocatalysts for clean energy-conversion, *Adv. Energy Mater.* 10 (2019), 1902844, <https://doi.org/10.1002/aenm.201902844>.
- [10] Z. Li, S.F. Ji, Y.W. Liu, X. Cao, S.B. Tian, Y.J. Chen, Z.G. Niu, Y.D. Li, Well-defined materials for heterogeneous catalysis: from nanoparticles to isolated single-atom sites, *Chem. Rev.* 120 (2020) 623–682, <https://doi.org/10.1021/acs.chemrev.9b00311>.
- [11] G. Humagain, K. MacDougall, J. MacInnis, J.M. Lowe, R.H. Coridan, S. MacQuarrie, M. Dasog, Highly efficient, biochar-derived molybdenum carbide hydrogen evolution electrocatalyst, *Adv. Energy Mater.* 8 (2018), 1801461, <https://doi.org/10.1002/aenm.201801461>.
- [12] L. Ma, Z. Bi, Y. Xue, W. Zhang, Q. Huang, L. Zhang, Y. Huang, Bacterial cellulose: an encouraging eco-friendly nano-candidate for energy storage and energy conversion, *J. Mater. Chem. A* 8 (2020) 5812–5842, <https://doi.org/10.1039/C9TA12536A>.
- [13] P.J. Guo, Z.Y. Xiong, S.Y. Yuan, K.H. Xie, H.J. Wang, Y.J. Gao, The synergistic effect of Co/CoO hybrid structure combined with biomass materials promotes photocatalytic hydrogen evolution, *Chem. Eng. J.* 420 (2021), 130372, <https://doi.org/10.1016/j.cej.2021.130372>.
- [14] H.Z. He, Y. Zhang, Y.Y. Li, P. Wang, Recent innovations of silk-derived electrocatalysts for hydrogen evolution reaction, oxygen evolution reaction and oxygen reduction reaction, *Int. J. Hydrog. Energy* 46 (2021) 7848–7865, <https://doi.org/10.1016/j.ijhydene.2020.11.265>.
- [15] H. Sun, Z. Yan, F. Liu, W. Xu, F. Cheng, J. Chen, Self-supported transition-metal-based electrocatalysts for hydrogen and oxygen evolution, *Adv. Mater.* 32 (2020), 1806326, <https://doi.org/10.1002/adma.201806326>.
- [16] X.Y. Zhang, J. Li, Y. Yang, S. Zhang, H.S. Zhu, X.Q. Zhu, H.H. Xing, Y.L. Zhang, B. L. Huang, S.J. Guo, E.K. Wang, Co₃O₄/Fe_{0.33}Co_{0.66}P interface nanowire for enhancing water oxidation catalysis at high current density, *Adv. Mater.* 30 (2018), 1803551, <https://doi.org/10.1002/adma.201803551>.
- [17] Q. Li, T. He, Y.-Q. Zhang, H. Wu, J. Liu, Y. Qi, Y. Lei, H. Chen, Z. Sun, C. Peng, L. Yi, Y. Zhang, Biomass waste-derived 3D metal-free porous carbon as a bifunctional electrocatalyst for rechargeable zinc-air batteries, *ACS Sustain. Chem. Eng.* 7 (2019) 17039–17046, <https://doi.org/10.1021/acssuschemeng.9b02964>.
- [18] Y. Wang, M. Jin, X. Zhang, C. Zhao, H. Wang, S. Li, Z. Liu, Direct conversion of biomass into compact air electrode with atomically dispersed oxygen and nitrogen coordinated copper species for flexible zinc-air batteries, *ACS Appl. Energy Mater.* 2 (2019) 8659–8666, <https://doi.org/10.1021/acsaem.9b01614>.
- [19] L. Xu, D.J. Deng, Y.H. Tian, H.P. Li, J.C. Qian, J.C. Wu, H.N. Li, Dual-active-sites design of CoNx anchored on zinc-coordinated nitrogen-codoped porous carbon with efficient oxygen catalysis for high-stable rechargeable zinc-air batteries, *Chem. Eng. J.* 408 (2021), 127321, <https://doi.org/10.1016/j.cej.2020.127321>.
- [20] L. Yang, X.F. Zeng, D. Wang, D.P. Cao, Biomass-derived FeNi alloy and nitrogen-codoped porous carbons as highly efficient oxygen reduction and evolution bifunctional electrocatalysts for rechargeable Zn-air battery, *Energy Storage Mater.* 12 (2018) 277–283, <https://doi.org/10.1016/j.ensm.2018.02.011>.
- [21] C.L. Lai, J.Y. Fang, X.P. Liu, M.X. Gong, T.H. Zhao, T. Shen, K.L. Wang, K. Jiang, D. L. Wang, In situ coupling of NiFe nanoparticles with N-doped carbon nanofibers for Zn-air batteries driven water splitting, *Appl. Catal. B Environ.* 285 (2021), 119856, <https://doi.org/10.1016/j.apcatb.2020.119856>.
- [22] Q.Y. Jin, B.W. Ren, H. Cui, C.X. Wang, Nitrogen and cobalt co-doped carbon nanotube films as binder-free trifunctional electrode for flexible zinc-air battery and self-powered overall water splitting, *Appl. Catal. B Environ.* 283 (2021), 119643, <https://doi.org/10.1016/j.apcatb.2020.119643>.
- [23] N.N. Xu, J.A. Wilson, Y.D. Wang, T.S. Su, Y.N. Wei, J.L. Qiao, X.D. Zhou, Y. X. Zhang, S.H. Sun, Flexible self-supported bi-metal electrode as a highly stable carbon- and binder-free cathode for large-scale solid-state zinc-air batteries, *Appl. Catal. B Environ.* 272 (2020), 118953, <https://doi.org/10.1016/j.apcatb.2020.118953>.
- [24] D.X. Ji, L. Fan, L.L. Li, S.J. Peng, D.S. Yu, J.N. Song, S. Ramakrishna, S.J. Guo, Atomically transition metals on self-supported porous carbon flake arrays as binder-free air cathode for wearable zinc-air batteries, *Adv. Mater.* 31 (2019), 1808267, <https://doi.org/10.1002/adma.201808267>.
- [25] L. Ma, S. Chen, Z. Pei, Y. Huang, G. Liang, F. Mo, Q. Yang, J. Su, Y. Gao, J. A. Zapien, C. Zhi, Single-site active iron-based bifunctional oxygen catalyst for a compressible and rechargeable zinc-air battery, *ACS Nano* 12 (2018) 1949–1958, <https://doi.org/10.1021/acsnano.7b09064>.
- [26] Z.H. Pan, J. Yang, W.J. Zang, Z.K. Kou, C. Wang, X.Y. Ding, C. Guan, T. Xiong, H. Chen, Q.C. Zhang, Y.T. Zhong, M.N. Liu, L.D. Xing, Y.C. Qiu, W.S. Li, C.L. Yan, Y. G. Zhang, J. Wang, All-solid-state sponge-like squeezable zinc-air battery, *Energy Storage Mater.* 23 (2019) 375–382, <https://doi.org/10.1016/j.ensm.2019.04.036>.
- [27] J. Balamurugan, T.T. Nguyen, N.H. Kim, D.H. Kim, J.H. Lee, Novel core-shell CuMo-oxynitride@N-doped graphene nanohybrid as multifunctional catalysts for rechargeable zinc-air batteries and water splitting, *Nano Energy* 85 (2021), 105987, <https://doi.org/10.1016/j.nanoen.2021.105987>.
- [28] P. Du, K.L. Hu, J. Lyu, H.L. Li, X. Lin, G.Q. Xie, X.J. Liu, Y. Ito, H.J. Qiu, Anchoring Mo single atoms/clusters and N on edge-rich nanoporous holey graphene as bifunctional air electrode in Zn-air batteries, *Appl. Catal. B Environ.* 276 (2020), 119172, <https://doi.org/10.1016/j.apcatb.2020.119172>.
- [29] H. Zhuo, Y.J. Hu, X. Tong, Z.H. Chen, L.X. Zhong, H.H. Lai, L.X. Liu, S.S. Jing, Q. Z. Liu, C.F. Liu, X.W. Peng, R.C. Sun, A supercompressible, elastic, and bendable carbon aerogel with ultrasensitive detection limits for compression strain, pressure, and bending angle, *Adv. Mater.* 30 (2018), 1706705, <https://doi.org/10.1002/adma.201706705>.
- [30] H.J. Son, M.J. Kim, S.H. Ahn, Monolithic Co-N-C membrane integrating Co atoms and clusters as a self-supporting multi-functional electrode for solid-state zinc-air batteries and self-powered water splitting, *Chem. Eng. J.* 414 (2021), 128739, <https://doi.org/10.1016/j.cej.2021.128739>.
- [31] C. Zhao, Y. Wang, Z. Li, W. Chen, Q. Xu, D. He, D. Xi, Q. Zhang, T. Yuan, Y. Qu, J. Yang, F. Zhou, Z. Yang, X. Wang, J. Wang, J. Luo, Y. Li, H. Duan, Y. Wu, Y. Li, Solid-diffusion synthesis of single-atom catalysts directly from bulk metal for efficient CO₂ reduction, *Joule* 3 (2019) 584–594, <https://doi.org/10.1016/j.joule.2018.11.008>.
- [32] Z. Yang, C. Zhao, Y. Qu, H. Zhou, F. Zhou, J. Wang, Y. Wu, Y. Li, Trifunctional self-supporting cobalt-embedded carbon nanotube films for ORR, OER, and HER triggered by solid diffusion from bulk metal, *Adv. Mater.* 31 (2019), 1808043, <https://doi.org/10.1002/adma.201808043>.
- [33] S.Y. Zhao, Y. Cheng, J.P. Veder, B. Johannessen, M. Saunders, L.J. Zhang, C. Liu, M.F. Chisholm, R. De Marco, J. Liu, S.Z. Yang, S.P. Jiang, One-pot pyrolysis method to fabricate carbon nanotube supported Ni single-atom catalysts with ultrahigh loading, *ACS Appl. Energy Mater.* 1 (2018) 5286–5297, <https://doi.org/10.1021/acsaem.8b00903>.
- [34] Z.L. Zhang, J. Cai, H. Zhu, Z.C. Zhuang, F.P. Xu, J.C. Hao, S.L. Lu, H.N. Li, F. Duan, M.L. Du, Simple construction of ruthenium single atoms on electropun nanofibers for superior alkaline hydrogen evolution: a dynamic transformation from clusters to single atoms, *Chem. Eng. J.* 392 (2020), 123655, <https://doi.org/10.1016/j.cej.2019.123655>.
- [35] L. Zhao, Y. Zhang, L.-B. Huang, X.-Z. Liu, Q.-H. Zhang, C. He, Z.-Y. Wu, L.-J. Zhang, J. Wu, W. Yang, L. Gu, J.-S. Hu, L.-J. Wan, Cascade anchoring strategy for general mass production of high-loading single-atomic metal-nitrogen catalysts, *Nat. Commun.* 10 (2019) 1278, <https://doi.org/10.1038/s41467-019-09290-y>.
- [36] Z. Zhang, J. Cai, H. Zhu, Z. Zhuang, F. Xu, J. Hao, S. Lu, H. Li, F. Duan, M. Du, Simple construction of ruthenium single atoms on electropun nanofibers for superior alkaline hydrogen evolution: a dynamic transformation from clusters to single atoms, *Chem. Eng. J.* 392 (2020), 123655, <https://doi.org/10.1016/j.cej.2019.123655>.
- [37] H.Y. Zou, G. Li, L.L. Duan, Z.K. Kou, J. Wang, In situ coupled amorphous cobalt nitride with nitrogen-doped graphene aerogel as a trifunctional electrocatalyst towards Zn-air battery driven full water splitting, *Appl. Catal. B Environ.* 259 (2019), 118100, <https://doi.org/10.1016/j.apcatb.2019.118100>.
- [38] C.Y. Su, H. Cheng, W. Li, Z.Q. Liu, N. Li, Z.F. Hou, F.Q. Bai, H.X. Zhang, T.Y. Ma, Atomic modulation of FeCo-nitrogen-carbon bifunctional oxygen electrodes for rechargeable and flexible all-solid-state zinc-air battery, *Adv. Energy Mater.* 7 (2017), 1602420, <https://doi.org/10.1002/aenm.201602420>.
- [39] A. Mukherjee, S. Banerjee, G. Halder, Parametric optimization of delignification of rice straw through central composite design approach towards application in grafting, *J. Adv. Res.* 14 (2018) 11–23, <https://doi.org/10.1016/j.jare.2018.05.004>.
- [40] C. Trilokesh, K.B. Uppuluri, Isolation and characterization of cellulose nanocrystals from jackfruit peel, *Sci. Rep.* 9 (2019) 16709, <https://doi.org/10.1038/s41598-019-53412-x>.
- [41] L. Zhong, H. Zhou, R. Li, H. Cheng, S. Wang, B. Chen, Y. Zhuang, J. Chen, A. Yuan, Co/CoO heterojunctions encapsulated N-doped carbon sheets via a dual-template-guided strategy as efficient electrocatalysts for rechargeable Zn-air battery, *J. Colloid Interface Sci.* 599 (2021) 46–57, <https://doi.org/10.1016/j.jcis.2021.04.084>.
- [42] N.-F. Yu, C. Wu, W. Huang, Y.-H. Chen, D.-Q. Ruan, K.-L. Bao, H. Chen, Y. Zhang, Y. Zhu, Q.-H. Huang, W.-H. Lai, Y.-X. Wang, H.-G. Liao, S.-G. Sun, Y.-P. Wu, J. Wang, Highly efficient Co₃O₄/Co@NCs bifunctional oxygen electrocatalysts for long life rechargeable Zn-air batteries, *Nano Energy* 77 (2020), 105200, <https://doi.org/10.1016/j.nanoen.2020.105200>.
- [43] M. Liu, J. Liu, Z. Li, F. Wang, Atomic-level Co₃O₄ layer stabilized by metallic cobalt nanoparticles: a highly active and stable electrocatalyst for oxygen reduction, *ACS Appl. Mater. Interfaces* 10 (2018) 7052–7060, <https://doi.org/10.1021/acami.7b16549>.
- [44] J. Yu, G. Chen, J. Sunarso, Y. Zhu, R. Ran, Z. Zhu, W. Zhou, Z. Shao, Cobalt oxide and cobalt-graphitic carbon core-shell based catalysts with remarkably high oxygen reduction reaction activity, *Adv. Sci.* 3 (2016), 1600060, <https://doi.org/10.1002/adv.201600060>.
- [45] C.-C. Hou, L. Zou, Q. Xu, A hydrangea-like superstructure of open carbon cages with hierarchical porosity and highly active metal sites, *Adv. Mater.* 31 (2019), 1904689, <https://doi.org/10.1002/adma.201904689>.
- [46] B.-Y. Xia, Y. Yan, N. Li, H.B. Wu, X.W. Lou, X. Wang, A metal-organic framework-derived bifunctional oxygen electrocatalyst, *Nat. Energy* 1 (2016) 15006, <https://doi.org/10.1038/nenergy.2015.6>.
- [47] J. Balamurugan, T.T. Nguyen, V. Aravindan, N.H. Kim, J.H. Lee, Highly reversible water splitting cell building from hierarchical 3D nickel manganese oxyphosphide nanosheets, *Nano Energy* 69 (2020), 104432, <https://doi.org/10.1016/j.nanoen.2019.104432>.

- [48] H.M. Sun, C.Y. Tian, G.L. Fan, J.N. Qi, Z.T. Liu, Z.H. Yan, F.Y. Cheng, J. Chen, C. P. Li, M. Du, Boosting activity on Co₄N porous nanosheet by coupling CeO₂ for efficient electrochemical overall water splitting at high current densities, *Adv. Funct. Mater.* 30 (2020), 1910596, <https://doi.org/10.1002/adfm.201910596>.
- [49] L.B. Wu, L. Yu, F.H. Zhang, B. McElhenny, D. Luo, A. Karim, S. Chen, Z.F. Ren, Heterogeneous bimetallic phosphide Ni₂P-Fe₂P as an efficient bifunctional catalyst for water/seawater splitting, *Adv. Funct. Mater.* 31 (2021), 2006484, <https://doi.org/10.1002/adfm.202006484>.
- [50] W.J. Hao, D.X. Yao, Q.Y. Xu, R.R. Wang, C.L. Zhang, Y.H. Guo, R.M. Sun, M. X. Huang, Z.L. Chen, Highly efficient overall-water splitting enabled via grafting boron-inserted Fe-Ni solid solution nanosheets onto unconventional skeleton, *Appl. Catal. B Environ.* 292 (2021), 120188, <https://doi.org/10.1016/j.apcatb.2021.120188>.
- [51] L.L. Yin, X. Du, C.Z. Di, M.W. Wang, K.M. Su, Z.H. Li, In-situ transformation obtained defect-rich porous hollow CuO@CoZn-LDH nanoarrays as self-supported electrode for highly efficient overall water splitting, *Chem. Eng. J.* 414 (2021), 128809, <https://doi.org/10.1016/j.cej.2021.128809>.
- [52] M.Q. Yao, H.H. Hu, B.L. Sun, N. Wang, W.C. Hu, S. Komarneni, Self-supportive mesoporous Ni/Co/Fe phosphosulfide nanorods derived from novel hydrothermal electrodeposition as a highly efficient electrocatalyst for overall water splitting, *Small* 15 (2019), 1905201, <https://doi.org/10.1002/sml.201905201>.
- [53] Z.K. Yang, C.M. Zhao, Y.T. Qu, H. Zhou, F.Y. Zhou, J. Wang, Y. Wu, Y.D. Li, Trifunctional self-supporting cobalt-embedded carbon nanotube films for ORR, OER, and HER triggered by solid diffusion from bulk metal, *Adv. Mater.* 31 (2019), 1808043, <https://doi.org/10.1002/adma.201808043>.
- [54] Z. Zhang, X. Zhao, S. Xi, L. Zhang, Z. Chen, Z. Zeng, M. Huang, H. Yang, B. Liu, S. J. Pennycook, P. Chen, Atomically dispersed cobalt trifunctional electrocatalysts with tailored coordination environment for flexible rechargeable Zn-air battery and self-driven water splitting, *Adv. Energy Mater.* 10 (2020), 2002896, <https://doi.org/10.1002/aenm.202002896>.
- [55] J. Balamurugan, T.T. Nguyen, N.H. Kim, D. Kim, J.H. Lee, Novel core-shell CuMo-oxynitride@N-doped graphene nanohybrid as multifunctional catalysts for rechargeable zinc-air batteries and water splitting, *Nano Energy* 85 (2021), 105987, <https://doi.org/10.1016/j.nanoen.2021.105987>.
- [56] Q. Shi, Q. Liu, Y. Ma, Z. Fang, Z. Liang, G. Shao, B. Tang, W.Y. Yang, L. Qin, X. S. Fang, High-performance trifunctional electrocatalysts based on FeCo/Co₂P hybrid nanoparticles for zinc-air battery and self-powered overall water splitting, *Adv. Energy Mater.* 10 (2020), 1903854, <https://doi.org/10.1002/aenm.201903854>.
- [57] H. Liu, J. Guan, S. Yang, Y. Yu, R. Shao, Z. Zhang, M. Dou, F. Wang, Q. Xu, Metal-organic framework-derived Co₂P nanoparticle/multi-doped porous carbon as a trifunctional electrocatalyst, *Adv. Mater.* 32 (2020), 2003649, <https://doi.org/10.1002/adma.202003649>.
- [58] H. Guo, Q.C. Feng, J.X. Zhu, J.S. Xu, Q.Q. Li, S.L. Liu, K.W. Xu, C. Zhang, T.X. Liu, Cobalt nanoparticle-embedded nitrogen-doped carbon/carbon nanotube frameworks derived from a metal-organic framework for tri-functional ORR, OER and HER electrocatalysis, *J. Mater. Chem. A* 7 (2019) 3664–3672, <https://doi.org/10.1039/c8ta11400e>.
- [59] B. Wang, L. Xu, G.P. Liu, P.F. Zhang, W.S. Zhu, J.X. Xia, H.M. Li, Biomass willow catkin-derived Co₃O₄/N-doped hollow hierarchical porous carbon microtubes as an effective tri-functional electrocatalyst, *J. Mater. Chem. A* 5 (2017) 20170–20179, <https://doi.org/10.1039/c7ta05002j>.
- [60] X.W. Zhong, W.D. Yi, Y.J. Qu, L.Z. Zhang, H.Y. Bai, Y.M. Zhu, J. Wan, S. Chen, M. Yang, L. Huang, M. Gu, H. Pan, B.M. Xu, Co single-atom anchored on Co₃O₄ and nitrogen-doped active carbon toward bifunctional catalyst for zinc-air batteries, *Appl. Catal. B Environ.* 260 (2020), 118188, <https://doi.org/10.1016/j.apcatb.2019.118188>.
- [61] S. Sultan, J.N. Tiwari, A.N. Singh, S. Zhumagali, M. Ha, C.W. Myung, P. Thangavel, K.S. Kim, Single atoms and clusters based nanomaterials for hydrogen evolution, oxygen evolution reactions, and full water splitting, *Adv. Energy Mater.* 9 (2019), 1900624, <https://doi.org/10.1002/aenm.201900624>.
- [62] C. Lei, Y. Wang, Y. Hou, P. Liu, J. Yang, T. Zhang, X. Zhuang, M. Chen, B. Yang, L. Lei, C. Yuan, M. Qiu, X. Feng, Efficient alkaline hydrogen evolution on atomically dispersed Ni-Nx Species anchored porous carbon with embedded Ni nanoparticles by accelerating water dissociation kinetics, *Energy Environ. Sci.* 12 (2019) 149–156, <https://doi.org/10.1039/C8EE01841C>.
- [63] L. Yan, Y. Xu, P. Chen, S. Zhang, H. Jiang, L. Yang, Y. Wang, L. Zhang, J. Shen, X. Zhao, L. Wang, A. Freestanding, 3D heterostructure film stitched by MOF-derived carbon nanotube microsphere superstructure and reduced graphene oxide sheets: a superior multifunctional electrode for overall water splitting and Zn-Air batteries, *Adv. Mater.* 32 (2020), 2003313, <https://doi.org/10.1002/adma.202003313>.
- [64] H. Xu, D. Wang, P. Yang, A. Liu, R. Li, Y. Li, L. Xiao, X. Ren, J. Zhang, M. An, Atomically dispersed M–N–C catalysts for the oxygen reduction reaction, *J. Mater. Chem. A* 8 (2020) 23187–23201, <https://doi.org/10.1039/D0TA08732G>.
- [65] X.R. Liu, X.Y. Fan, B. Liu, J. Ding, Y.D. Deng, X.P. Han, C. Zhong, W.B. Hu, Mapping the design of electrolyte materials for electrically rechargeable zinc-air batteries, *Adv. Mater.* 33 (2021), 2006461, <https://doi.org/10.1002/adma.202006461>.
- [66] T. Liu, J.R. Mou, Z.P. Wu, C. Lv, J.L. Huang, M.L. Liu, A facile and scalable strategy for fabrication of superior bifunctional freestanding air electrodes for flexible zinc-air batteries, *Adv. Funct. Mater.* 30 (2020), 2003407, <https://doi.org/10.1002/adfm.202003407>.
- [67] D. Ji, L. Fan, L. Tao, Y. Sun, M. Li, G. Yang, T.Q. Tran, S. Ramakrishna, S. Guo, The Kirkendall effect for engineering oxygen vacancy of hollow Co₃O₄ nanoparticles toward high-performance portable zinc-air batteries, *Angew. Chem. Int. Ed.* 58 (2019) 13840–13844, <https://doi.org/10.1002/anie.201908736>.
- [68] C.L. Lai, M.X. Gong, Y.C. Zhou, J.Y. Fang, L. Huang, Z.P. Deng, X.P. Liu, T.H. Zhao, R.Q. Lin, K.L. Wang, K. Jiang, H.L. Xin, D.L. Wang, Sulphur modulated Ni₃FeN supported on N/S co-doped graphene boosts rechargeable/flexible Zn-air battery performance, *Appl. Catal. B Environ.* 274 (2020), 119086, <https://doi.org/10.1016/j.apcatb.2020.119086>.